Experimental and numerical modelling of sedimentation in a rectangular shallow basin

Sameh A. KANTOUSH[1], Erik BOLLAERT[2], and Anton J. SCHLEISS[3]

Abstract

  Numerical simulation of flows in shallow reservoirs has to be checked for its consistency in predicting real flow conditions and sedimentation patterns. Typical flow patterns may exhibit flow separation at the inlet, accompanied by several recirculation and stagnation areas all over the reservoir surface. The aim of the present research project is to study the influence of the geometry of a reservoir on sediment transport and deposition numerically and experimentally, focusing on a prototype reservoir depth between 5 and 15 m as well as suspended sediment transport.

  A series of numerical simulations is presented and compared with scaled laboratory experiments, with the objective of testing the sensitivity to different flow and sediment parameters and different turbulence closure schemes. Different scenarios are analyzed and a detailed comparison of preliminary laboratory tests and some selected simulations are presented.

  The laboratory experiments show that suspended sediment transport and deposition are determined by the initial flow pattern and by the upstream and downstream boundary conditions. In the experiments, deposition in the rectangular basin systematically developed along the left bank, although inflow and outflow were positioned symmetrically along the centre of the basin. Three major horizontal eddies developed influencing the sediment deposition pattern. Although asymmetric flow patterns are privileged, a symmetric pattern can appear from time to time.

  This particular behaviour could also be reproduced by a two-dimensional depth-averaged flow and sediment transport model (CCHE2D). The paper presents numerical simulations using different turbulence closure schemes (k-ε and eddy viscosity models). In spite of the symmetric setup, these generally produced an asymmetric flow pattern that can easily switch sides depending on the assumptions made for the initial and boundary conditions. When using the laboratory experiment as a reference, the most reliable numerical results have been obtained with a parabolic depth-averaged eddy viscosity model. This model appeared to be the only one that was able to reproduce the strongly asymmetric flow behaviour observed during the experiments.

Key Words: Shallow reservoir sedimentation and morphology, Suspended sediment, Reservoir geometry influence, Numerical simulations, Scaled physical modelling

1 Introduction

  Shallow flows can be defined as predominantly horizontal flows in a fluid domain where the vertical dimension is significantly smaller than the two horizontal dimensions. By using this assumption, the basic flow equations can be simplified following a normalization procedure (Stoker, 1957). This leads to the

---

[1] Dr., Corresponding author, Ecole Polytechnique Fédérale de Lausanne (EPFL), Laboratory of Hydraulic Constructions (LCH), Station 18, CH -1015 Lausanne, Switzerland, E-mail: sameh.kantoush@epfl.ch.
[2] Dr., Ecole Polytechnique Fédérale de Lausanne (EPFL), Laboratory of Hydraulic Constructions (LCH), Station 18, CH -1015 Lausanne, Switzerland, E-mail: erik.bollaert@epfl.ch.
[3] Prof., Ecole Polytechnique Fédérale de Lausanne (EPFL), Laboratory of Hydraulic Constructions (LCH), Station 18, CH -1015 Lausanne, Switzerland, E-mail: anton.schleiss@epfl.ch.

shallow water equations (SWE), which are the common points of the various applications. There are several supplementary parameters which may be negligible or not, leading to variants of the shallow-water equations (SWE). Shallow flow models play an important role in hydraulic, environmental, river, and coastal engineering.

 In bounded shear flows, the 3-D turbulent eddy size is typically limited to the shortest dimension (in this case the water depth). Hence, large-scale, two dimensional coherent turbulent structures with length-scales orders of magnitude greater than the depth are observed in a wide range of shallow shear flows. These structures are important for controlling momentum and constituent transport (Chen and Jirka, 1995) and appear to result from instabilities of quasi-two-dimensional shear flow (Chen and Jirka, 1997).

 Turbulent shallow flows are studied experimentally in Chu & Babarutsi (1988), Uijttewaal et al. (2000), Balachandar et al. (2000 and 2001).

 The use of scaled laboratory models to investigate shallow flow processes is restricted, mainly because of too low Reynolds numbers and too high Froude numbers at small scales. A compromise has to be made between desired shallowness and model feasibility. Often the chosen compromise is hardly shallow (e.g. river models with width to depth ratios of 2 to 4, instead of ratios of between 50 and a few hundred as found in real rivers). Booij (1986, 2003) measured shallow flows in a series of harbours of various forms. The goal was to investigate the dependence of the flow in the harbour entrance on its form, the layout of its entrance and on the shallowness. The measurements show that in a shallow harbour the flow is concentrated along the sides, whereas in a not sufficiently shallow harbour the water rotates as a whole. Shallowness plays a role in the development of the mixing layer at the harbour, entrance through which momentum is exchanged between river and harbour. Chu and Babarutsi (1988) showed that in shallow flow the development of the mixing layer is suppressed. Reservoir sedimentation rates have first been predicted by using empirical curves relating the reservoir capacity loss with basic hydrodynamic parameters (Churchill, 1948; Brune, 1953; Brown, 1958). The distribution of sediment deposits was also addressed (Heinemann, 1961; Graf, 1983).

 The present study focuses on sedimentation of shallow reservoirs with a prototype depth of between 5.0 and 15.0 m. A reservoir is thereby defined as an artificial lake into which water drains and is stored for future use. Sometimes, a reservoir is created by damming of existing natural lakes to improve their capacity. The behaviour of sediments in a shallow reservoir is mainly determined by bed morphology and main 2D water circulation, as well as by the characteristics of the sediment. Recent laboratory experiments and numerical simulations for a wide flume (Sloff et al., 2004) showed that channel formation in shallow reservoirs is highly dependent on the boundary and the initial flow conditions and the reservoir geometry. Based on the state-of-the-art, existing research on shallow reservoir sedimentation does not consider the influence of the geometry of the reservoir on the sedimentation process by suspension. The presently ongoing research focuses on the influence of the geometry of shallow reservoirs on the settling of suspended particles. The first objective of the experiments is to gain insight into the governing physical processes. The influence of 2D shallow turbulent flow structures on bed morphology will be investigated. Moreover, a better understanding of the sediment exchange process between the jet entering the reservoir and the associated turbulence structures is studied. The experiments should also allow determining the "ideal" reservoir geometry, defined as the one that minimizes the settlement of suspended sediments. Finally, comparison between laboratory experiments and numerical models should allow validating of the latter.

2 Physical modelling

2.1 Experimental setup

 Comprehensive information on similitude requirements for movable and fixed bed models can be found in Yalin (1970) and Kobus (1980). Scaled physical models are based on a similarity theory, which uses a series of dimensionless parameters that fully or at the least, partially characterize the physics. The choice of a scaling factor $\lambda=Lp/Lm$, or length scale ratio, to be used in the experiments, is determined by the objectives of the research. According to the length of the tested section and laboratory constraints, the present laboratory model has been designed with horizontal and vertical scales of $\lambda_l = \lambda_h = 50$ (Kantoush et al., 2005). Model similarity is shown in Table 1.

The experiments were carried out in a specific test facility at the Laboratory of Hydraulic Constructions (LCH) of the Swiss Federal Institute of Technology (EPFL). A schematic view of the experimental setup is shown in Fig. 1. The setup consists of a rectangular inlet channel, 0.25 m wide and 1.0 m long, made of PVC, a rectangular shallow basin with inner dimensions of 6.0 m long and 4.0 m wide, a rectangular outlet channel 0.25 m wide and 1.0 m long, and finally a flap gate 0.25 m wide and 0.30 m high at the end of the outlet. The bottom and the walls of the basin are made of 15mm thick PVC plates. The basin is 0.30 m deep and has a flat bottom. Adjacent to the reservoir, a mixing tank is used to prepare and store the water-sediment mixture. A sediment supply tank is mounted above the mixing tank. The mixing tank is equipped with a propeller type mixer to create a homogenous sediment concentration. To control the sediment concentration, a small gate is installed at the lower end of the sediment supply tank. This tank is attached to a vibrating device with variable speed to control sediment release. The water-sediment mixture is drained by gravity into the water-filled rectangular basin through a flexible pipe with a diameter of 0.10 m. Along the basin side walls, a 4.0 m long, movable, aluminium frame is mounted which carries the measurement instruments.

Table 1 Characteristic values of prototype and model (model scale 1:50)

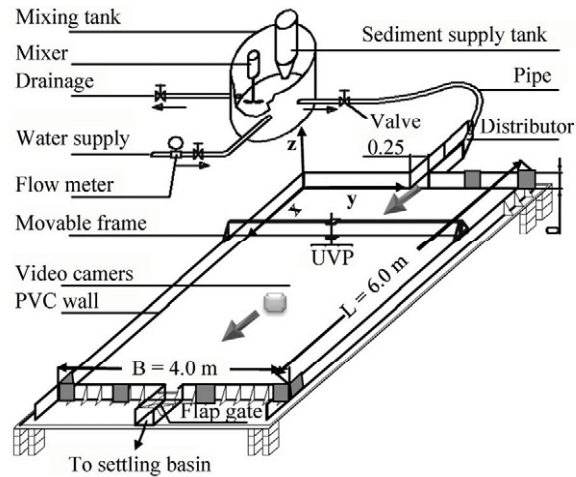| Item	Dimension	Prototype	Model
Basin length L	(m)	300	6
Basin width B	(m)	200	4
Water depth h	(m)	10	0.2
Bottom roughness n	$(s/m^{1/3})$	0.025	0.012
Mean flow velocity V	(m/s)	0.85	0.12
Particle diameter, d_{50}	(mm)	0.05	0.05
Mean fall velocity, ω	(m/s)	0.03	0.001
Min/Max discharge Q	(m^3/s)	62.5/125	0.0035/0.007
Suspended sediment concentration C_s	(g/l)	9	3
Bottom slope J	(−)	1%	Horizontal

Fig. 1 Schematic view of the experimental installation

2.1.1 Experimental conditions

To ensure a uniform mixture in the mixing tank and reservoir basin, the density of the sediment mixture as well as the clear water are measured before and during the test by means of a turbidity meter. To model suspended sediment currents in the laboratory model, crushed walnut shells with a median grain size d_{50}=50µm, density 1,500 kg/m^3 was used in all tests. These are non cohesive and light grains (Fig. 2). The sediments were added to the mixing tank during the tests. The hydraulic conditions were chosen to fulfil the sediment transport requirements (Table 1). Furthermore, for all tests, Froude number was small

enough and Reynolds number high enough to ensure subcritical, fully developed turbulent flow conditions.
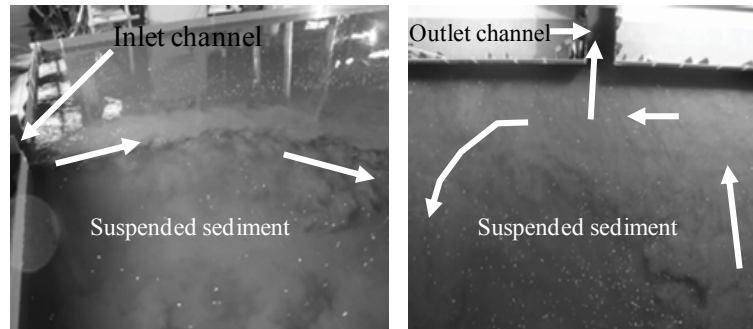

Fig. 2 Left: mixture entering the basin; Right: mixture exiting the basin

2.2 Measurements and data acquisition system

Several parameters were measured during every test; namely: surface velocities, deposited sediment layer thickness, suspended sediment concentration at the outlet, 3D flow velocity, water level and water temperature. Table 2 provides an overview of the measurements and instrumentations used during the tests.

Table 2 Model parameters and instrumentation

Measured parameters	Dimension	Instrument
Water level	(m)	Ultrasonic probe
Sediment thickness	(m)	Mini Echo sounder (UWS)
Discharge	(m³/s)	Flow meter
Flow velocity	(m/s)	Ultrasound velocity profiler (UVP)
Surface velocity	(m/s)	Large Scale Particle Image Velocimetry (LSPIV)
Temperature	(Cº)	Thermistors
Sediment concentration	(g/l)	Turbidity meter

2.2.1 Ultrasonic Doppler Velocity Profiler (UVP)

The velocities were measured by means of an Ultrasonic Doppler Velocity Profiler (Metflow SA, UVP-DUO), which allows instantaneous measurement of the 1D velocity profile over depth (Metflow, 2002). The measurement probes were mounted on a support in groups of three, allowing determining the local 3D flow field (Fig. 3). Since the number of measurement points was high, four groups of three 1D profiles (constituting one 3D profile) are simultaneously recorded to accelerate data acquisition. To cover the whole cross section of the basin, 4 positions were chosen along the cross section; each position has four groups of three probes (Fig. 3). All twelve probes were mounted on a frame which moves in the two horizontal directions. The probes were inclined at 20° to the vertical and have an emitting frequency of 2 MHz. A multiplexer (Fig. 3) allowed switching between the different UVP-probes. Velocity profiles were recorded for all points on a 25cm by 50 cm grid (transversal and flow directions respectively). To extract the 3D velocity field in twelve cross sections over the whole reservoir, the acquired binary velocity file needed some treatment. First the twelve 1D records were read from the raw data file. Then the time-averaged velocity components (average of 24 profiles) are derived. Then projection for these values and obtained velocity components cover the whole measurement depth. After rearrangement of the velocity profile, the data was exported to a text file for future automatic treatment with Matlab.
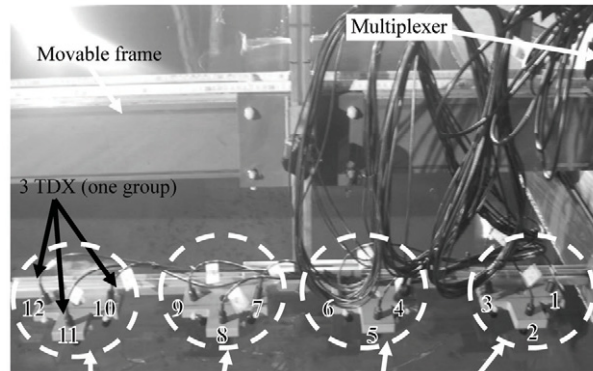
Fig. 3 Scheme of UVP installation

2.2.2 Large-Scale Particle Velocimetry (LSPIV)

Large-scale particle image velocimetry (LSPIV) is an efficient and powerful technique for measuring river surface velocities. LSPIV is an extension of conventional PIV for velocity measurements in large-scale flows. While the image and data-processing algorithms are similar to those used in conventional PIV, adjustments are required for illumination, seeding, and pre-processing of the recorded images. Planar in water column flow measurements with PIV are described for instance in Adrian (1991). In hydraulic engineering, this technique has so far mainly been applied for surface velocity measurements of water and ice in very uniform flow fields as well as in groyne field experiments (Ettema et al., 1997; Fujita et al., 1998; Weitbrecht et al., 2002). PIV measurements have not yet been applied to define detailed flow patterns in differently shaped shallow reservoirs on rivers.
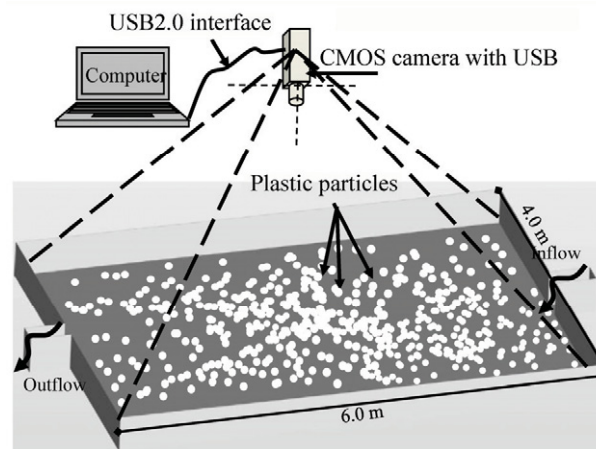

Fig. 4 Scheme of LSPIV installation

A digital camera was used to record the images. The camera was fixed above the basin covering an area of 4.0 m by 5.0 m (Fig. 4), i.e. a length of 0.5 m was missing at the upstream and downstream ends. The recorded images were systematically transformed to remove perspective distortion from the objective lens using PTLens software and then processed using FlowManager software.

Seeding was obtained by means of white plastic particles and reasonable lights as shown in Fig. 4. The plastic particles had an average diameter of 3.4 mm and a specific weight of 960 kg/m^3. The dispersed light allowed recording their positions at two successive instants by means of a video camera (SMX-155, monochrome, 1.3 megapixels). The plan view (measurement plan) was divided into several sub-areas, known as interrogation areas, (IA). In each IA, a cross-correlation algorithm was applied in order to compute the shift ΔX of the particles during the time ΔT between two images.

2.2.3 Mini Echo Sounder (UWS)

The bed morphology was measured by means of a miniature echo sounder (Ultralab UWS). The sounder works with an ultrasonic-impulse-run time procedure. UWS first emits an acoustic signal. The transmitted ultrasound impulse is then reflected on any object that serves as a target. This acoustic reflection (echo) propagates in the space and is received by the ultrasound sensor. To measure the effective distance between target and sensor, at first the run-time which the sound needs from the sensor must be determined and then the run time for the signal from the sensor to the target and back to the sensor again must be determined. Knowing the run time and the sound velocity, the target distance can be computed. The sounder was mounted on the movable frame (Fig. 5) and scanned the whole basin area. The measured cross sectional profiles were generally 0.05 m apart. In some cases, a 0.025 m spacing was tested, starting and ending at 0.10 m from the basin side walls, i.e. covering a width of 4.0 m. The measured longitudinal profiles were spaced 0.20 m apart. In some cases, a 0.1 m spacing was tested, starting and ending at 0.05 m from the up- and downstream boundaries.
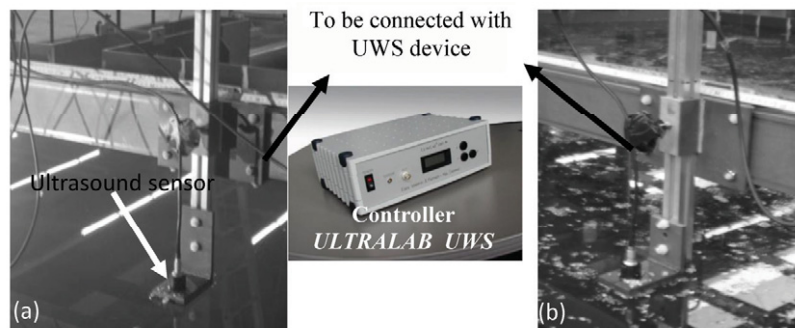
Fig. 5 (a) Miniature echo sounder mounted on the frame measuring the initial surface with clear water (before sediment deposition) (b) Miniature echo sounder mounted on the frame measuring after sediment deposition

During the tests, the discharge was automatically recorded by an electromagnetic flow meter. The precision is 1% of the maximum flow scale, corresponding to 0.2 l/s.

2.3 Test program

The followed test program and experimental runs are detailed at Table 3. For practical reasons, most tests were performed with a total duration of 4.5 hours. Nevertheless, to account for progressive morphological evolution and verify final formation of dynamic equilibrium, some long-term tests have been performed with durations of up to 18 hours.

It has to be noticed that these longer runs were performed in several 4.5 hour steps, i.e. the facility has been arrested every 4.5 hours to allow bed morphology recording.

2.4 Test procedure

One hour after starting the pump and stabilizing the flow for a given discharge, the LSPIV measurements are performed for the case of clear water traversing the basin. Sediment is then added to the sediment supplier tank and the sediment concentration which enters the mixing tank is verified. UVP probes measure 1D vertical velocity profiles as well as local 3D velocities. Every 20 minutes, the bed morphology is measured at different cross sections. Every 30 minutes, PIV measurements are performed.

2.5 Experimental results

The characteristics of the experimental tests with a rectangular basin are summarized in Table 3. A total discharge of 7.0 l/s, a flow depth of 0.20 m and a sediment concentration of 3.0 g/l has been used as boundary and initial conditions.

Table 3 Characteristics of experimental tests

Test No.		1	2	3	4
Geometry form					
Dimension	Width [m]	4.0	4.0	4.0	4.0
	Length [m]	6.0	6.0	6.0	6.0
Hydraulic conditions	H: Water depth [m]	0.2	0.2	0.2	0.2
	Q_w: Water discharge [l/s]	7.0	7.0	7.0	7.0
	J: Slope [%]	0.0	0.0	0.0	0.0
	Re: Reynolds number [−]	15,000	15,000	15,000	15,000
	Fr: Froude number [−]	0.1	0.1	0.1	0.1
Suspended sediment conditions	d_{50} [mm]	0.05	0.05	0.05	0.05
	$U*/\omega$ [−]	1.3	1.3	1.3	1.3
	Z: Suspension number [−]	2.1	2.1	2.1	2.1
	ρ_s: Sediment density [kg/m^3]	1,500	1,500	1,500	1,500
Sediment transport	Sediment in suspension	Up to water depth	Up to water depth	Up to water depth	Up to water depth
	Q_s: sediment discharge [kg/hr]	75.0	75.0	75.0	75.0
	C_s: Sediment concentration [g/l]	3.0	3.0	3.0	3.0
	V_d: Deposited sediment volume [m^3]	0.5476	0.5188	0.5244	2.5216
Time	T_t: Total run time [hr]	4.5	4.5	4.5	18
	T_c: Run time continuous [hr]	1.5, 1.5, and 1.5	1.5, 1.5, and 1.5	4.5	4.5, 4.5, and 9
	N_{Stop}: No of stopping pump	3.0	3.0	1.0	3.0
Measurements	UWS: Mini echo sounder	Used after every stop	Used after every stop	Used after every stop	Used after every stop
	UVP: Ultrasound Velocity Profiler	Used in the first 1.5 hrs	Used in the second 1.5 hrs	Not used	Not used
	Flow rate: Electromagnetic meter	Working all time	Working all time	Working all time	Working all time
	Temperature: Thermostat	Working all time	Working all time	Working all time	Working all time
	US: Water level	Working all time	Working all time	Working all time	Working all time
	LSPIV: Surface velocity	Every 30 minutes	Every 30 minutes	Every 30 minutes	Every 30 minutes

2.5.1 Flow field

The time-averaged flow fields recorded by using LSPIV and UVP measurements are depicted in Figs. 6 and 7. At the start of the test (t=0h), a plane jet issues from the narrow leading channel and enters into the much wider basin. After jet issuance, the main flow tends to go towards the right hand side, generating a large and stable main gyre, rotating anticlockwise, and two small 'triangular' gyres, rotating clockwise in the two upstream corners of the basin. The jet appears to be attracted to one of the side-walls. Its preference for the right side is weak, since a stable mirror image of the flow pattern can easily be established by slightly adapting the initial conditions. By following floating particles, it is noticed that, starting from the entrance, the particle path goes straight ahead and, in the next two meters, it deflects to the right until it stagnates against the centre of the right wall. Particles that do not leave the basin through the outlet channel circulate with the main gyre and reach a separation zone along the left side wall. A small gyre has formed at the downstream left corner of the basin. This circulation pattern is self-sustainable because of the inertia of the main gyre that pushes the incoming jet aside. An initially smooth bottom favours this inertia dominated pattern. The flow structures measured by UVP and LSPIV (Figs. 6 and 7) are similar in magnitude and have the same gyre centres.
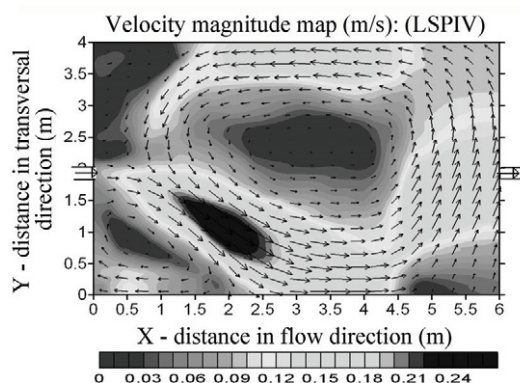
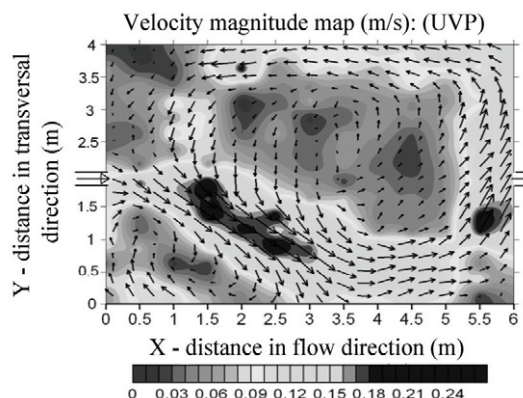**Fig. 6** Flow field recorded by LSPIV   **Fig. 7** Flow field recorded by UVP

After 1.5 hours of sediment feeding (t=1.5h), the observed flow pattern did not differ much from the starting one, except for the increase in size of the right corner gyre and a downstream shifted reattachment point along the right sidewall. The later phenomena are probably related to the suspended sediment deposits and the associated bed morphology.

2.5.2 Morphological changes

The final bed morphology (after 1.5 hours) by means of bed elevation contours shows two morphological features were observed. The first one was a local ripple formation. This occurred first along the right hand side and later on during the test along the centreline. The second observed feature was global sediment deposition throughout the basin. The deposits were mainly concentrated on both right and left sides of the basin, with rather low deposits in the centre of the basin. The abovementioned flow patterns are clearly visible in the bed morphology.

The resistance to flow is relatively small for the smooth and plane bed at the start. However, the flow resistance increases as morphological structures develop on the bed. Most of the sediment deposits take place near the right side wall. The interaction between bed forms and flow patterns is clearly very complex. The strong dynamic behaviour of the bed morphology seems to indicate that a much longer run would be necessary to reach dynamic equilibrium of the bed.

As a conclusion on the above described laboratory experiment, it may be stated that both flow and sediment patterns were strongly asymmetric, although all test parameters (inflow, outflow, bottom level) were in perfect symmetry with the centreline of the basin. This phenomenon is known in aerodynamics as the "Coanda effect", proving that the flow and sediment patterns are very sensitive to boundary and initial conditions. Furthermore, the experiment points out the strong interaction between flow patterns and bed morphological development.

3 Numerical modelling

Numerous equations for predicting suspended transport rates are available in the literature, and a good review is given by (Dyer and Soulsby, 1988). They pointed out that one of the principal differences between various suspended transport equations lies in the forms chosen to represent the distribution of eddy viscosity and eddy diffusivity. However, after examination of a number of representative eddy viscosity expressions, including constant, linear and parabolic depth-dependent distributions, they concluded that all distributions, except the constant distribution, result in similar sediment transport rates.

Computational models generally make use of sediment transport formulas and a one-dimensional (1-D) backwater profile calculation (Graf, 1983). Two-dimensional (2D) vertical-averaged models solve the vertical sediment concentration profiles, allowing for more precision in the near-bed particle exchange flux calculation. However, existing 2D models do not specifically address the present problem of shallow reservoirs (van Rijn, 1987; Lai and Shen, 1996). A comparison of most commercially and academic

available computational models can be found in Langendoen (2001), who gives a fairly detailed description of their features to evaluate them.

3.1 Used computational model

The computational model used here is the CCHE2D model, developed by NCCHE (National Center for Computational Hydroscience and Engineering).

CCHE2D (Jia and Wang, 1999; Wu, 2001) is a depth-integrated 2D hydrodynamic and sediment transport model based on a variant of the finite element method. The model is used to predict river flow patterns and related bed and/or bank erosion for both uniform and non-uniform sediment transport. Both depth-averaged k–ε and eddy viscosity turbulence closures are available. The effects of secondary flow in curved channels on the bed-load direction are modelled, but not the effects on fluid momentum and sediment transport rate. The rate and direction of the bed-load transport is adjusted according to the bed slope.

CCHE2D was used for its capabilities to simulate suspended sediment transport. Suspended transport occurs mostly at a non-equilibrium state and is usually simulated by non-equilibrium transport models. CCHE2D implements a full non-equilibrium transport model for bed-material load (bed load plus suspended load). Non-equilibrium approaches are proposed for cases where sediment transport occurs mainly as bed load, as suspended load, or as full total load, respectively. Also, the model simulates the transport of non-uniform sediment mixtures with multiple size classes. Several formulas for fractional non-cohesive sediment transport capacity and movable bed roughness are provided. CCHE2D is freeware code and detail description of this governing equations and features can be found in Wu (2001). Lots of formulas are available for fractional non-cohesive sediment transport. CCHE2D code proposes four sediment transport capacity formulas accounting for the hiding and exposure effects of non-uniform sediment are always considered. The sediment transport capacity is determined by van Rijn's (1984) formula, Wu et al's (2000) formula, SEDTRA module (Garbrecht et al., 1995), the modified Ackers and White's formula (Proffit and Sutherland, 1983), or the modified Engelund and Hansen's formula (Wu and Vieira, 2000). The SEDTRA module uses three different formulas to calculate sediment transport capacities for different size ranges: (Laursen's, 1958) formula for size classes from 0.01 to 0.25 mm, (Yang, 1973) formula for size classes from 0.25 to 2.0 mm, and (Meyer-Peter and Mueller's, 1948) Formula for size classes from 2.0 to 50.0 mm. The required initial conditions include the initial channel geometry and initial bed material gradation. For a complete simulation of sediment transport, information on sediment properties, sediment transport capacity, non-equilibrium adaptation length and movable bed roughness should be given.

The sediment properties include the sediment grain size, specific gravity (default value: 2.65), grain shape factor (default value: 0.7) and bed material porosity. The sediment transport capacity, non-equilibrium adaptation length and the movable roughness are determined by empirical formulas.

3.2 Results of numerical computations

Numerical simulations have been performed to test the sensitivity of the different model parameters and to compare them with the laboratory experiment. The results are described hereafter. According to the laboratory model; a simple rectangular basin has been simulated. This basin has a rectangular grid spacing of 0.05 m in both flow and transverse directions. For turbulence closure three different models were used namely; Depth-Integrated Parabolic Model (DIPM), Depth-Integrated Mixing Length Model (DIMLM), and k-ε model (Jia and Wang, 2001; Wu, 1989). For DIPM the eddy viscosity v_t is calculated by the following formula:

$$v_t = \frac{A_{xy}}{6} \kappa U^* h \tag{1}$$

where A_{xy} is an adjustable coefficient of eddy viscosity, κ is the von Karman constant, and U^* is the shear velocity. Table 4 shows descriptions of numerical runs and values of parameters used.

3.2.1 Boundary conditions

In the depth-averaged 2-D simulation of sediment transport, the inflow sediment discharge must be given at each inlet boundary. The numerical simulations are summarized in Table 4. They are compared

with the numerical reference simulation A-2, for which boundary conditions and further details are summarized in Table 5. For the sediment transport calculation, the inflow sediment discharges.

To reduce the complexity of the system, specific processes such as sediment sorting are not included for the moment.

Table 4 Characteristics of numerical simulations

Series	Run N°	Turbulence closure	Characteristic features	Parameters			
				A_{xy} [−]	d_{50} [m]	δ_m [m]	t [hr]
A	A-1	DIPM	Different turbulence closure models were used: DIPM, DIMLM, κ-ε.	1			
	A-2	DIPM	A_{xy} varies for series A and B.	50			
	A-3	DIPM		150			
B	B-1	DIMLM		2			
	B-2	DIMLM		20			
C	C	κ-ε					
D	D-1	DIPM	Two different grain sizes		0.00009		
	D-2	DIPM			0.00015		
M	M-1	DIPM	Mixing layer thickness δ_m varies			0.025	
	M-2	DIPM				0.05	
	M-3	DIPM				0.1	
L	L-1	DIPM	Long time runs				1.5
	L-2	DIPM					3
	L-3	DIPM					4.5
	L-4	DIPM					9
MO	MO-1	DIPM	Clear water flow on a movable bed which developed from Run A-2, erosion of the developed bed.				1.5
	MO-2	DIPM					65
	MO-3	DIPM					133

3.3 Parametric analysis

The analysis is according to Table 4 hereafter. The sensitivity of the parameters is discussed hereafter. Beside the simulations referenced in Table 4, some further runs are also discussed.

3.3.1 Turbulence closure influence

Three types of turbulence closures were used in run series A, B, and C. Depth-integrated parabolic and mixing length based on eddy viscosity models were used in run series A and B. Both eddy viscosity models were tested for a wide range of values of the adjustable coefficient A_{xy} (values between 1 and 1000). The output values were defined for a 1.5 hrs run time. The presentation of the results uses the following procedure:

1. For each model and for different parametric values, four figures are shown: velocity magnitude, kinematic eddy viscosity, suspended sediment concentration and bed elevation.
2. A longitudinal section has been taken along the basin centre line.

3.3.1.1 Run series A

A depth-integrated parabolic eddy viscosity model was used, with A_{xy} ranging from 1, 2 … to 1000. Results are presented for A_{xy} = 1, 50, and 150. Figure 8 shows the results of Run A-1 where (A_{xy} = 1). Figure 8a presents the velocity magnitudes and vectors. The water-sediment mixture flows from the narrow inlet channel into the much wider basin. At first, the inflow mixture behaves like a jet that remains quite separated from the clear water in the basin. After some distance, the shear between both bodies of water moving at different speeds causes mass and momentum exchange and thus eddies are peeled off from the core of the jet. This peeling off occurs alternatively on both sides of the jet and generates eddies that increase in size with longitudinal distance. Furthermore, the jet starts to undulate with a wavelength and amplitude that increase with longitudinal distance. This behaviour resembles a continuously growing

instability. Figure 8b shows the kinematic eddy viscosity. As the eddy viscosity is directly related to the shear velocity, its behaviour is similar to velocity (Fig. 8a).

Table 5 Boundary conditions for reference run (simulation A-2)

| Boundary conditions	Symbol	Value	Dimension
Water discharge	Q_w	0.007	(m³/s)
Downstream water level	h	0.2	(m)
Sediment concentration	Q_s	4	(kg/m³)
Sediment density	ρ_s	1500	(kg/m³)
Sediment diameter	d_{50}	0.00005	(m)
Sediment porosity	p	0.4	(−)
Wall boundary condition	-		
Bottom slope	J	0	(%)
Model			
Basin width	B	4	(m)
Basin length	L	6	(m)
Grid spacing	Δx	0.05	(m)
Width/length of inlet channel	$b/l_{,in}$	0.25/1.0	(−)
Width/length of outlet channel	$b/l_{,out}$	0.25/1.0	(−)
Manning roughness coefficient	n	0.015	(s/m^{1/3})
Modelling parameters			
Mixing layer thickness	δ_m	0.05	(m)
Adaptation length for bed load	l_s	0.35	(m)
Adaptation factor for suspended load	α	0.2	(−)
Transport mode	Total load as suspended load		
Transport capacity formula	Wu et al. (2000)		
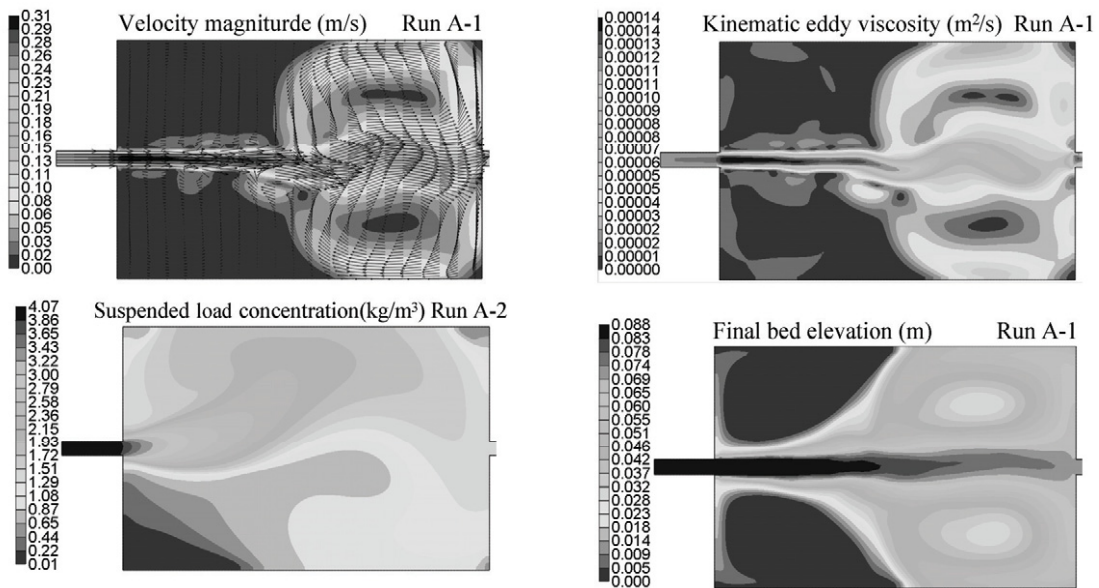
Fig. 8 Results for numerical simulation run A-1: a) stationary flow field with velocity vectors and magnitudes, b) kinematic eddy viscosity, c) suspended load concentration, and d) final bed elevation results

From the lowest to the highest flow velocities in the basin, the eddy viscosity changes by up to one order of magnitude. Figure 8c presents the suspended sediment distribution. The initial concentration in the inlet channel equals 3.0 kg/m³. This concentration diffuses throughout the basin following the general velocity and eddy viscosity pattern described above. Nevertheless, the sediment concentration pattern

does not undulate as much as velocity and remains more or less symmetric. Finally, Fig. 8d shows the final bed elevations after 4.5 hours of testing. Similar to the sediment concentration distribution, the bed change remains symmetric and shows maximum values of up to 0.09 m, i.e. about 45 % of the initial water depth.

Figure 9 shows the results for run A-2. The eddy viscosity parameter has a value of $A_{xy} = 50$, resulting in viscosities 50 times higher than the first run. Figure 9a presents the simulated stationary flow field with velocity magnitudes and vectors. In contrast with the flow pattern of Run A-1, the flow pattern computed here is found to agree fairly well with the experimental observations (Figs. 6 and 7), showing the incoming jet deflecting towards the left-hand side of the basin, combined with a large eddy on the right-hand side and a small eddy in the left corner of the upstream part of the reservoir. The jet apparently diffuses much faster than for run A-1 in Fig. 8a.
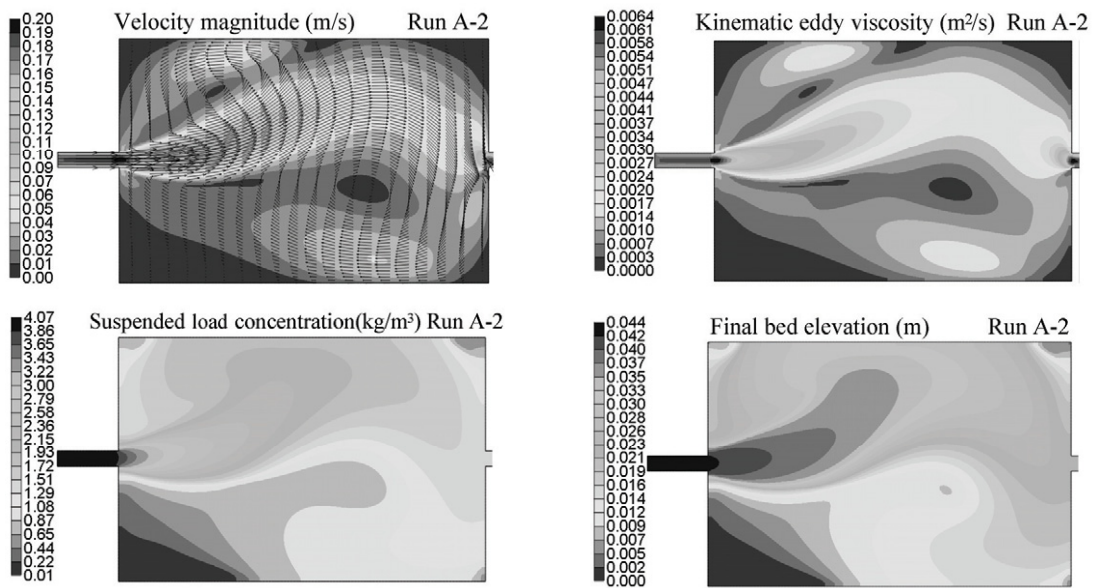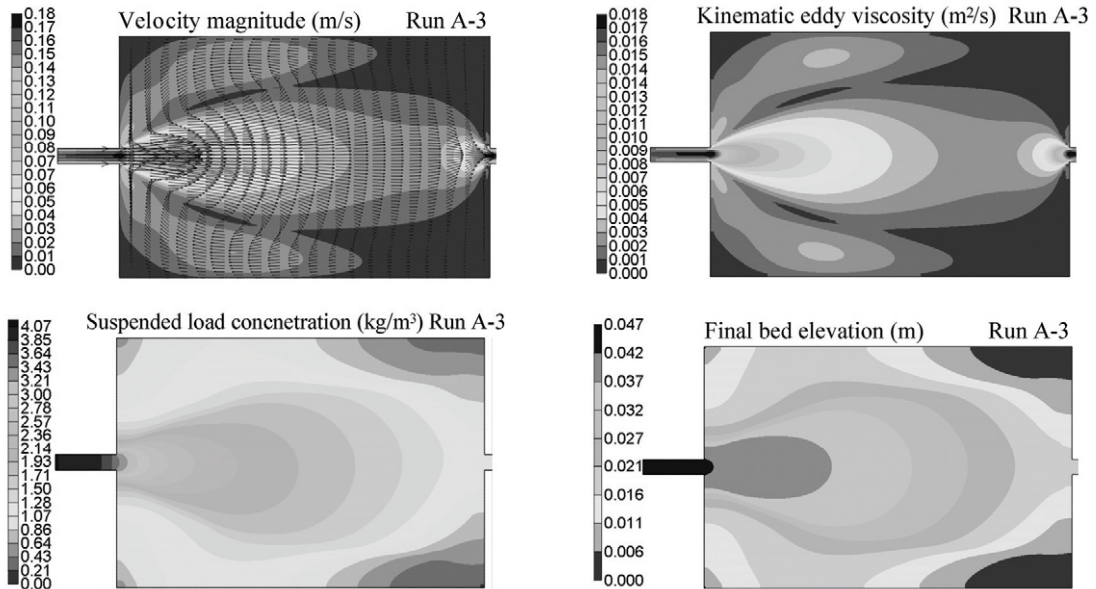

Fig. 9 Results for numerical simulation run A-2: a) stationary flow field with velocity vectors and magnitudes, b) kinematic eddy viscosity, c) suspended load concentration, and d) final bed elevation results.

It was found that this flow pattern can switch to a reverse pattern with the jet positioned on the right-hand side and the eddy along the left-hand side. This could be numerically achieved by changing the initial state or the local geometry of the reservoir. The kinematic eddy viscosity presented in Fig. 9b follows the same pattern and diffuses much faster. By further increasing A_{xy}, towards 150, small eddies start to form at each corner of the basin, similar to the eddy that is observed in run A-2 along the left hand side of the reservoir for $A_{xy} = 50$. For A_{xy} more than 150, the flow starts to become more and more symmetric, with two small eddies at the entrance reservoir corners as shown in Fig. 10a for run A-3. Finally, for A_{xy} between 500 and 1000 four small eddies are generated at each corner of the basin. The morphology in Fig. 9d (Run A-2) shows that the flow pattern concentrates the depositions on the left hand side. Figure 10 shows the results for Run A-3 with $A_{xy} = 150$. The flow pattern in Fig. 10a shows symmetric behaviour with two small eddies in both corners near the entrance of the reservoir and a centralized jet flow that diffuses very fast. Similarly, the kinematic eddy viscosity, the suspended sediment concentration and sediment depositions are highest along the centreline of the basin and reduce towards the sides as shown in Figs. 10b–10d. It can be concluded that with higher values of the kinematic eddy viscosity, the flow and sediment deposition behave in a quasi-symmetric manner.

The mirrors of flow pattern and bed deformation shown in Fig. 9 are most similar to those observed in the laboratory experiments. The corresponding range of A_{xy} values is situated between 20 and 120. Hence, when using the laboratory experiments as a reference, using a depth-integrated parabolic eddy viscosity

model, with eddy viscosities between 0.001 m²/s and 0.006 m²/s, seems to provide the qualitatively most plausible results.

Fig. 10 Results for numerical simulation run A-3: a) stationary flow field with velocity vectors and magnitudes, b) kinematic eddy viscosity, c) suspended load concentration, and d) final bed elevation results.
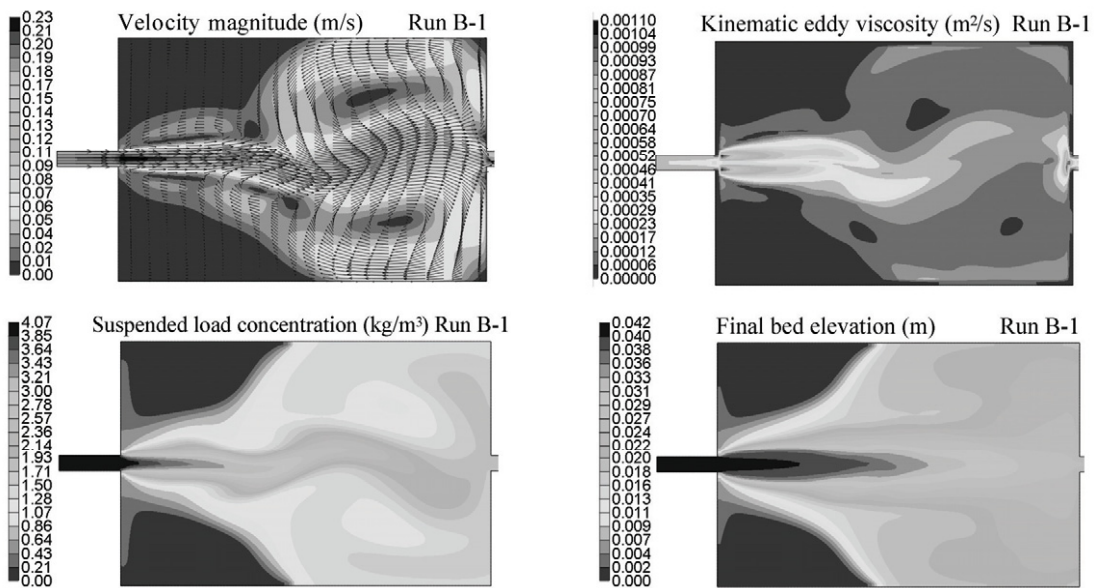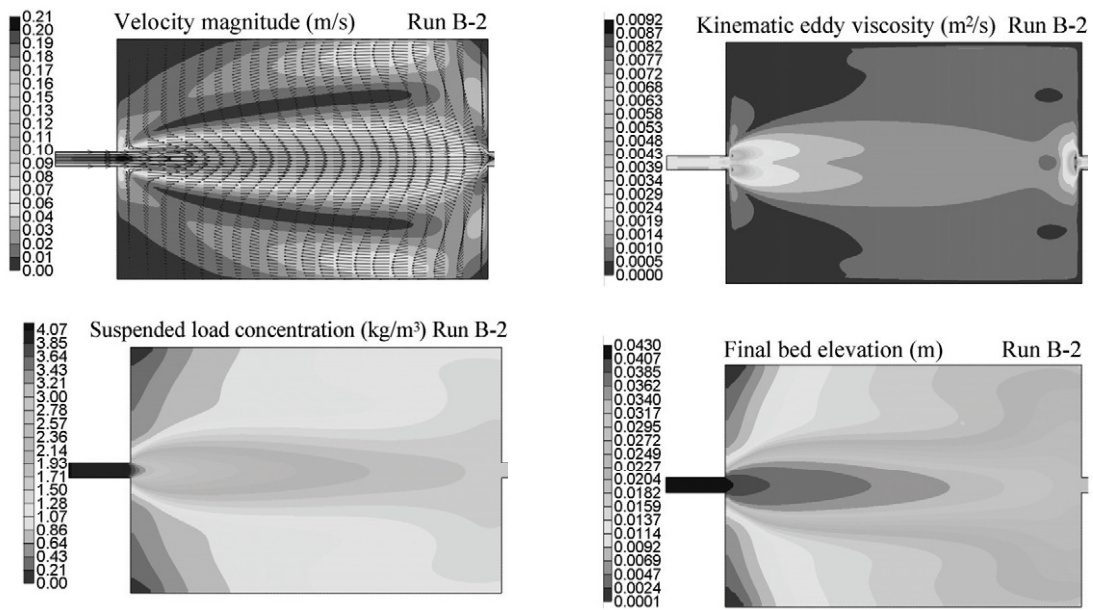

Fig. 11 Results for numerical simulation run B-1: a) stationary flow field with velocity vectors and magnitudes, b) kinematic eddy viscosity, c) suspended load concentration, and d) final bed elevation results.

3.3.1.2 Run series B

Series B uses a depth-integrated mixing layer model (hereafter; DIMLM). Figures 11 and 12 present the results of Runs B-1 and B-2 respectively. Analysis of these runs is quite similar to the one performed for run series A. Several simulations have been carried out with A_{xy} values varying between 1 and 100. Figures 11 and 12 show the results for A_{xy} = 2 and 20 respectively. The lowest value thereby generates

flow and sedimentation patterns very similar to the ones observed for run A-1. The highest value is very similar to the results obtained for run A-3. As a first-hand conclusion, the DIMLM turbulence closure model seems less suitable to reproduce the flow and sediment patterns observed during the laboratory experiment.

3.3.1.3 Run series C

Run series C uses the two-equation k-ε turbulence model. Figure 13a shows the velocity magnitude and vectors and Fig. 13b the corresponding kinematic eddy viscosity. It was found that two large recirculation eddies develop along both sides of the basin. The flow pattern is perfectly symmetric and differs from the experimental one shown in Figs. 6 and 7.

Fig. 12 Results for numerical simulation run B-2: a) stationary flow field with velocity vectors and magnitudes, b) kinematic eddy viscosity, c) suspended load concentration, and d) final bed elevation results.

3.3.1.4 Comparison of run series along the basin centreline

Figures 14 to 18 present a detailed comparison of velocity magnitude, kinematic eddy viscosity, suspended sediment concentration, and final bed elevation along the basin centreline of all previous run series. Velocity distributions for run series A, B, and C are similar in the inlet channel. At the interface between inlet channel and basin, a sudden velocity increase occurs, followed by a gradual decrease throughout the whole basin length (Fig. 14).
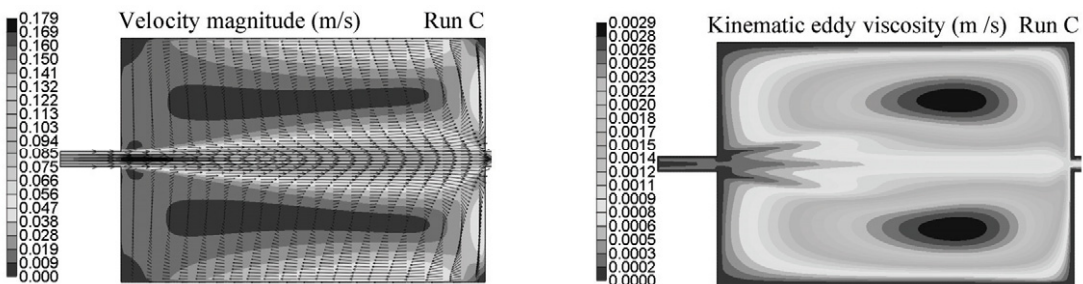

Fig. 13 Results for numerical simulation run C: a) stationary flow field with velocity vectors and magnitudes, b) kinematic eddy viscosity.

For low eddy viscosities (runs A-1 and B-1), the velocity trace agrees with the flow pattern meandering along the centreline. At the outlet of the basin, all runs exhibit similar flow behaviour: at 0.50 m upstream of the outlet section, the velocity progressively increases towards a peak value at the outlet section itself, followed by a small decrease and finally stabilization of the velocity profile inside the outlet channel. The appearance of the peak value is generated by the sudden geometric change, which generates a weak plunging water surface at the constriction and thus increasing velocity values. The centreline velocity inside the basin decreases with increasing eddy viscosity (run series A-2 and A-3).
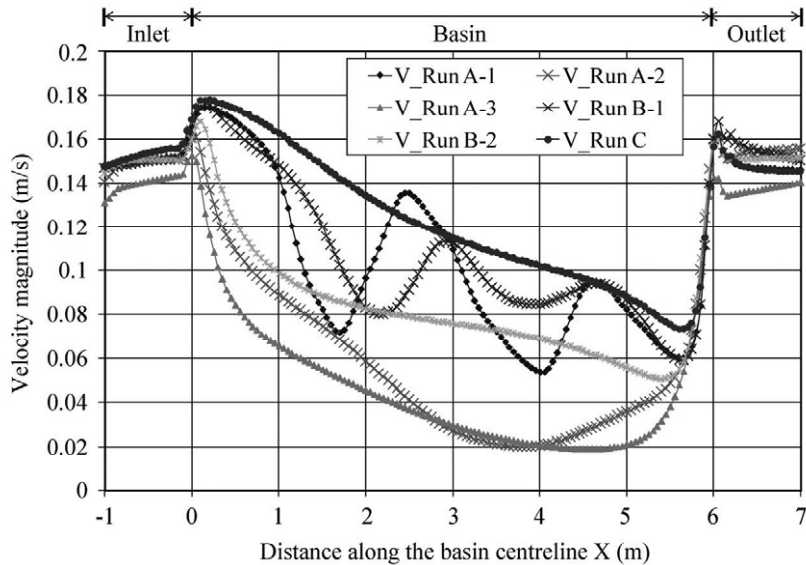
Fig. 14 Comparison of depth-averaged velocity magnitude along basin centreline
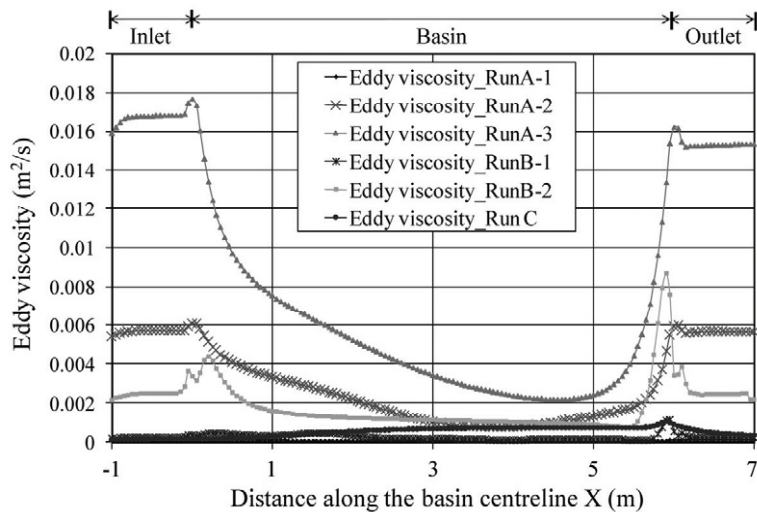for run series A, B, and C

Fig. 15 Comparison of kinematic eddy viscosity along basin centreline
for run series A, B, and C

Figure 15 compares the longitudinal changes in eddy viscosity for runs A, B, and C, while Fig. 16 shows a comparison between the predicted bed profiles for runs A-2, A-3, B-1, and B-2 along the centre line of the basin. For run A-2, the influence of the flow deviating towards the left-hand side of the basin is clearly visible by strongly reduced bed thickness. Also, due to the recirculation eddy, the sediment

deposits gradually start to increase again in front of the outlet. Figure 17 shows similar trends for the suspended sediment concentration along the centreline of the basin, with, run A-2 exhibiting a low suspended sediment concentration in the middle of the basin. Moreover, for run B-1, the sediment concentration oscillates in the middle of the basin.
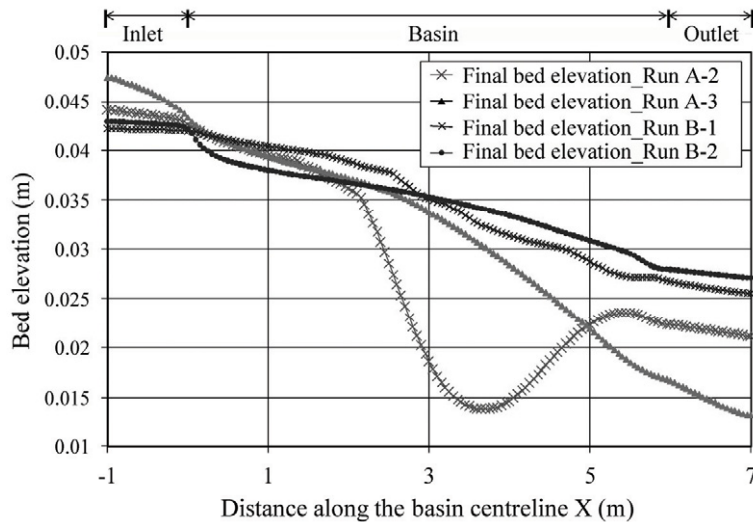

Fig. 16 Comparison of bed profiles along basin centreline for run series A and B
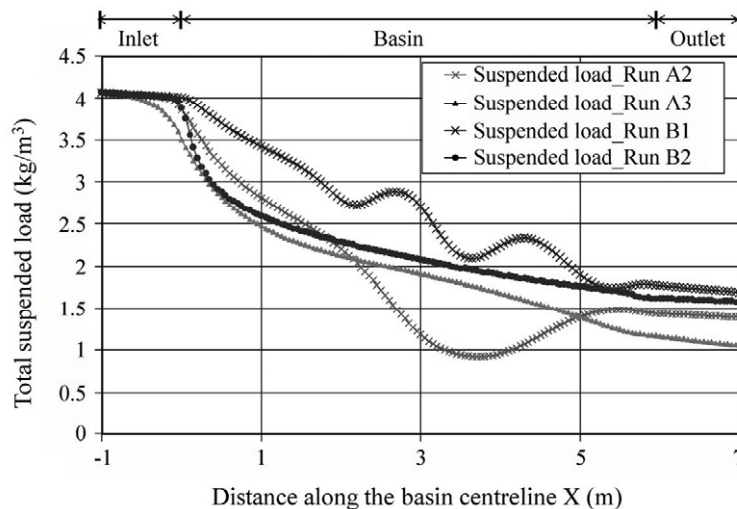

Fig. 17 Comparison of suspended load concentration along basin centreline
for run series A and B

3.3.2 Grain size distribution influence

Two different simulations have been conducted with a modification of the grain size curve towards extreme grain sizes, with the sediment inflow rate being the similar to the one used during the reference laboratory experiment. The turbulence model used is the Depth-Integrated Parabolic Model (DIPM). Hence, run D-1 uses $d_{50} = 0.09$ mm and run D-2 $d_{50} = 0.15$ mm. Figure 18 compares the resulting bed profiles along the centreline of the basin. Despite the fact that the final bed morphology was expected to be different, both results were found to be similar. The reason for this is not clear yet, but might be due to the relatively short duration of the runs (only 1.5 h). Longer duration experiments will be performed in the near future.
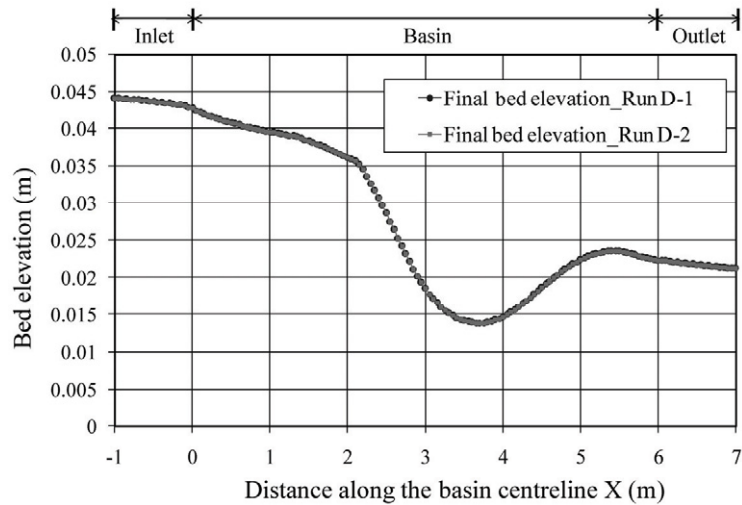
Fig. 18 Comparison of bed profiles along basin centreline for run series D

3.3.3 Bottom layer thickness influence

The mixing layer represents that part of the sediment at the bed that can be exchanged with the sediment transported by the flow. The bed material gradation usually varies with the vertical direction, so the bed material above the non-erodible layer is divided into several layers, as shown in Fig. 19. The top layer is the mixing layer, whereas the second one is the subsurface layer. The variation of bed material gradation in the mixing layer is determined by (Wu, 1991)

$$\frac{\partial(\delta_m p_{bk})}{\partial t} = \frac{\partial z_{bk}}{\partial t} + p_{bk}^* \left(\frac{\partial \delta_m}{\partial t} - \frac{\partial z_b}{\partial t} \right) \tag{2}$$

where p_{bk} is the bed material gradation in the mixing layer; δ_m is the thickness of the mixing layer, which is related to the flow and sediment conditions as well as the bed deformation; $\partial z_b / \partial t$ is the total bed deformation rate, $\partial z_b / \partial t = \sum_{k=1}^{N} \partial z_{bk} / \partial t$; N is the total number of size classes; p_{bk}^* is p_{bk} when, $\partial \delta_m / \partial t - \partial z_b / \partial t \le 0$ and p_{bk}^* is the bed material gradation in the subsurface layer when $\partial \delta_m / \partial t - \partial z_b / \partial t \succ 0$.

The bed material gradations in the layers under the mixing layer are determined by using the mass conservation law.

Fig. 19 Multiple-layer sorting model of bed material gradation

The objective of run series M is to test the sensitivity of the model to this exchangeable control volume. M-1, M-2, and M-3 were performed with mixing layer thicknesses of 0.025, 0.05 and 0.1 m respectively. For numerical reasons (i.e., deposition during a one time step should not exceed mixing layer thickness), the time step has been reduced proportionally for these runs. Figure 20 shows the bed elevation along the centreline of the basin for the three runs. By increasing the mixing layer thickness till ¼ of the water

depth, bed elevation increases see Fig. 20 for curve M1 and M2. But for higher values of the mixing layer (half of the water depth bed elevation decreases as shown in Fig. 21 for curve M3 which overlaps with curve M1.
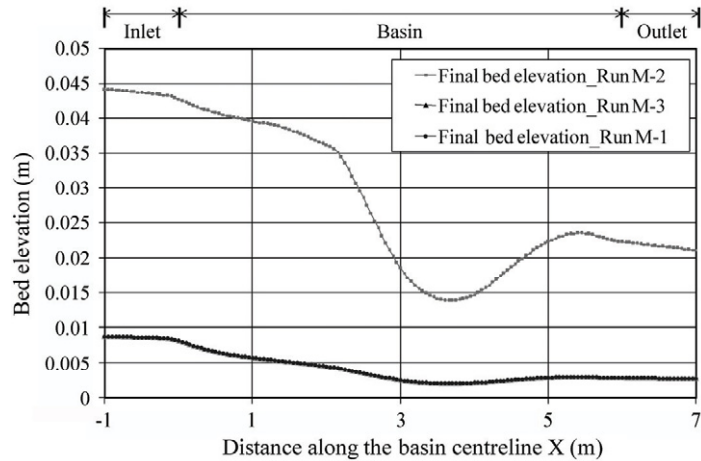

Fig. 20 Comparison of bed profiles along basin centreline for run series M

3.3.4 Run time duration influence

Figure 21 shows the evolution of the sediment depositions at different run time periods (1.5 hrs, 3.0 hrs, 4.5 hrs, and 9.0 hrs) along the centreline of the basin. The figure shows almost constant bed thickness within the first time period. Bed thickness increases and is less homogenous along the centreline after 3.0 and 4.5 hours. Beds become thicker and even more irregular after 9.0 hours. It may be concluded that a stable morphology has not yet been reached after 9.0 hours and that longer runs would be needed to attain morphological equilibrium in the basin.
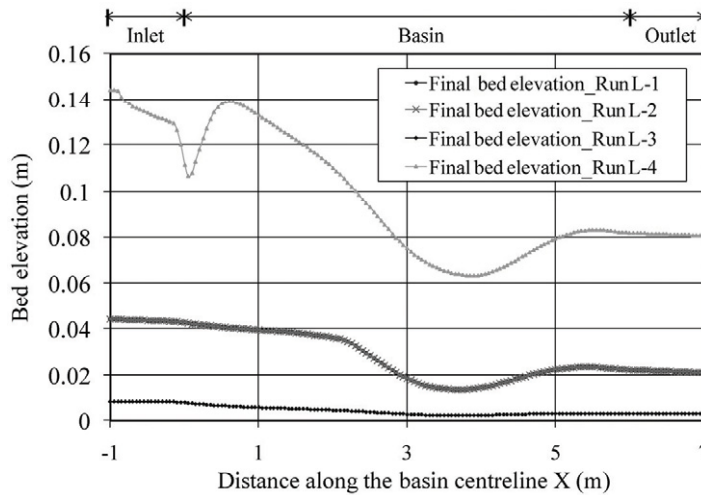

Fig.21 Comparison of bed profiles along basin centreline for run series L

3.3.5 Movable bed influence

The bed morphology obtained for run B-2 was used as initial bathymetry for run series MO as shown in Fig. 22. Clear water without sediment was injected into the basin to investigate the bed evolution for MO1, MO2, and MO3 at different time periods (1.5 hrs, 65 hrs and 133 hrs). Between 65 and 133 hrs, no significant change is observed anymore between the respective bed profiles. Hence, for these flow and sediment conditions, the basin might be close to its morphological equilibrium.

As a conclusion, A_{xy} has a significant effect on flow patterns, velocity distributions, sediment concentrations and bed forms.
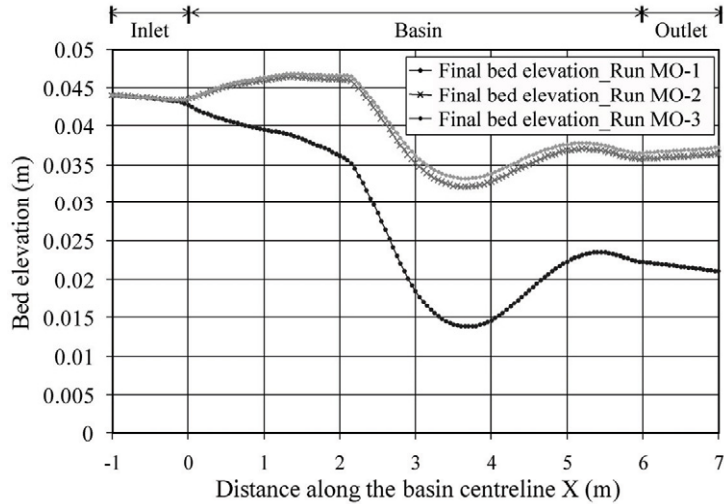

Fig. 22 Comparison of bed profiles along basin centreline for run series MO

4 Comparison of experimental and numerical results

A detailed comparison of flow field and morphological development between the experimental model and numerical simulation Run A2 is presented.

4.1 Flow map

Figure 23 shows that the numerically computed velocity vectors are acceptable and generally in a good agreement with the experimentally observed vectors.
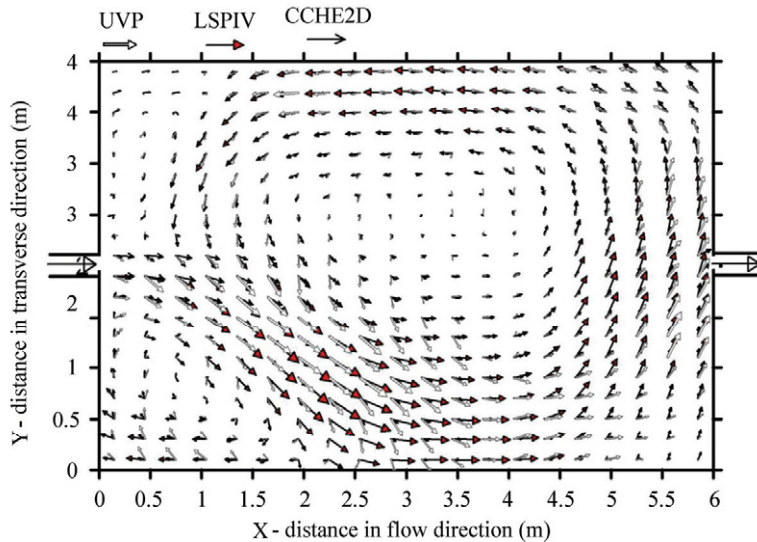

Fig. 23 Comparison of velocity magnitude vectors recorded by UVP and LSPIV
with numerically simulated velocity magnitude vectors (run A-2)

Figure 24 compares the computed and measured axial velocity magnitude at the basin centreline. In the inlet channel, experimentally observed velocity distributions are approximately the same. At the interface between inlet channel and basin, a sudden velocity increase is observed in the computations, followed by a gradual decrease throughout the whole basin length.
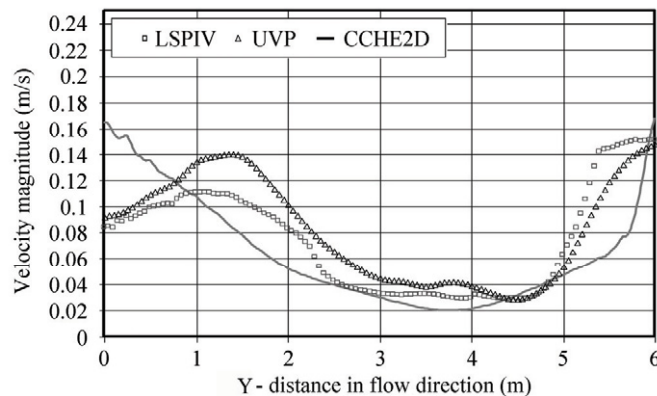
Fig. 24 Comparison of depth-averaged velocity magnitude recorded by UVP and
LSPIV with numerically simulated velocity magnitude (run A-2).
Longitudinal profile is taken along basin centreline.

5 Conclusions

First results of ongoing research on the influence of the geometry of a shallow reservoir on suspended sediment transport and deposition have been presented. Comparison has been made between a laboratory experiment and depth-averaged numerical simulations. The experimentally observed flow patterns and bed morphological developments have been recorded by means of UVP and LSPIV techniques. The numerical simulations have been performed by means of a freeware 2D depth-averaged model allowing for non-equilibrium suspended load transport. During both experimental and numerical modelling, it was found that the flow patterns are quite sensitive to boundary and initial conditions. Also, strongly asymmetric flow and morphological patterns frequently developed during the experiments. These patterns could be simulated numerically by use of a parabolic eddy viscosity model.

Analysis of these the first-hand experiments allowed the following observations:

(1) The two-dimensional velocity vector field for shallow reservoirs can be reconstructed by combining three measurement data sets of UVP.

(2) LSPIV allows adequate velocity measurements in shallow water flow problems.

References

Adrian R. J. 1991, Particle-imaging techniques for experimental fluid mechanics. Annu. Re. Fluid Mech. 23, pp. 261–304.

Balachandar R., Ramachandran S., and Tachie M. F. 2000, Characteristics of shallow turblent near wakes at low Reynolds numbers. Journal of Fluids Engineering 122, pp. 302–308.

Balachandar R. and Tachie M. F. 2001, A study of boundary layer-wake interaction in shallow water layer. Fluid Dynamics Research 16, pp. 511–521.

Booij R. 1986, Metingen van uitwisselingen tussen haven en rivier. (in Dutch). Rep. 9-86, section Hydr. Engrg. Dep. Civil Engrg., Delft Univ. of Technology.

Booij R. 2003, Measurements and large eddy simulations of the flows in some curved flumes. Journal of turbulence 4(March 2003) 008.

Brune G. M. 1953, Trap efficiency of reservoirs. Trans. Am. Geoph. Union, Vol. 34, No. 3.

Brown C. B. 1958, Sediment transportation. In H. Rouse(ed.). Engineering hydraulics, Wiley, New York.

Chen D. and Jirka G. H. 1995, Experimental study of boundary layer-wake interaction in shallow water layer. Fluid Dynamics Research 16, pp. 11–41.

Chen D. and Jirka G. H. 1997, Absolute and convective instabilities of plane turbulent wakes in a shallow water layer. Journal of Fluid Mechanics 338, pp. 157–172.

Chu V. H. and Babarutsi S. 1988, Confinement and bed-friction effects in shallow turbulent mixing layer. Journal of Hydraulic Engineering 114, pp. 1257–1274.

Churchill M. A. 1948, Discussion of analysis and use of reservoir sedimentation data by L.C. Gottchalk, Proc. of Federal Inter-Agency Sedimentation Conference, Washington DC., pp. 139–140.

Dyer K. R. and Soulsby R. L. 1988, Sand transport on the continental shelf. Ann. Rev. Fluid Mech., 20, pp. 295–324.

Emttea R., Fujita I., Muste M., and Krufer A. 1997, Particle image velocimetry for whole field measurement of ice velocities. Cold Regions Science and Technology 26, pp. 97–112.

Fujita I., Muste M., and Kruger A. 1998, Large scale particle image Velocimetry for flow analysis in hydraulic engineering applications, Journal of hydraulic Research, 36, pp. 397–414.

Garbrecht J., Kuhnle R., and Alonso C. 1995, A sediment transport capacity formulation for application to large channel networks. Journal of Soil and Water Conservation, Vol. 50, No. 5, pp. 527–529.

Graf W. H. 1983, The hydraulics of reservoir sedimentation. Int. Water Power and Dam Construction. Vol. 35, No. 4, pp. 45–52.

Heineman H. G. 1961, Sediment distribution in small flood retarding reservoirs in the Missouri Basin Loess Hills. Agricultural Research Service, pp. 41–44.

Jia Y. and Wang S. S. Y. 1999, Numerical model for channel flow and morphological change studies. Journal of Hydraulic. Eng. Vol. 125, No. 9, pp. 924–933.

Jia Y. and Wang S. S. Y. 2001, CCHE2D: Two-dimensional Hydrodynamic and Sediment Transport Model for Unsteady Open Channel Flows Over Loose Bed. Technical Report No. NCCHE-TR-2001-1, National Center for Computational Hydroscience and Engineering, The University of Mississippi, USA.

Kantoush S. A., Bollaert E. F. R., Boillat J.-L., and Schleiss A. J. 2005, Suspended load transport in shallow reservoirs. Final Proc. XXXI IAHR Congress. Korea Water Resources Association, Seoul, South Korea, pp. 1787–1799.

Kobus H. 1980, Hydraulic Modeling. Pitman, Boston, Mass.

Lai J. S. and Shen H. W. 1996, Flushing sediment through reservoirs. Journal of Hydraulic Research, Vol. 34, No. 2, pp. 237–225.

Langendoen E. J. 2001, Evaluation of the effectiveness of selected computer models of depth-average free surface flow and sediment transport to predict the effects of hydraulic structures on river morphology. Rep., prepared for WES Vicksburg, National Sedimentation Laboratory, Agricultural Research Service, U. S. Department of Agriculture, Vicksburg, Miss.

Laursen E. 1958, The total sediment load of streams. Journal of Hydraulic Div., Am. Soc. Civ. Eng., Vol. 54, No. 1, pp. 1–36.

Metflow. 2002, UVP Monitor Model UVP-DUO- Users guide. July 2002, Metflow SA, Lausanne, Switzerland.

Meyer-Peter E. and Mueller R. 1948, Formulas for bed-load transport. Rep. on 2nd meeting of IAHR, Stockholm, Sweden, pp. 39–64.

Proffit G. T. and Sutherland A. J. 1983, Transport of non-uniform sediment. Journal of Hydraulic Research, 21, pp. 33-43.

Sloff C. J., Jagers H. R. A., and Kitamura Y. 2004, Study on the channel development in a wide reservoir. Proc. of River Flow, Napoli, Italy, pp. 811-819.

Stoker J. J. 1957, Water waves. The mathematical theory with applications.

Uijttewaal W. S. J., Lehmann D., and Mazijk A. van. 2001, Exchange processes between a river and its groyne fields: Model experiments. J. Hydr. Engrg. Vol. 127, No. 11, pp. 928–936.

van Rijn, L. C. 1984a, Sediment transport, part I: bed load transport. Journal of Hydraulic Eng., ASCE, Vol. 110, No. HY10, pp. 1431–1456.

van Rijn L. C. 1984b, Sediment transport, part III: bed forms and alluvial roughness. Journal of Hydraulic Engineering, ASCE, Vol. 110, No. HY12, pp. 1733–1754.

van Rijn L. C. 1987, Mathematical modeling of morphological processes in the case of suspended sediment transport. Delft Hydraulics Communication No. 382, Delft Hydraulics Laboratory, Delft, The Netherlands, 208.

Weitbrecht V., Kühn G., and Jirka G. H. 2002, Large scale PIV-measurements at the surface of shallow water flows. Flow Meas. and Instr, 13, pp. 237–245.

Wu W. 1991, The Study and Application of 1-D, Horizontal 2-D and Their Nesting Mathematical Models for Sediment Transport. PhD., Dissertation, Wuhan University of of Hydraulic and Electric Engineering, China.

Wu W. 1989, Hydraulic properties of reservoir desilting. Proc. 23rd IAHR Congress, Ottawa, Canada.

Wu W., Rodi W., and Wenka Th. 2000, 3D numerical modeling of flow and sediment transport in open channels. Journal of Hydraulic Engineering, ASCE, Vol. 126, No. 1, pp. 4–15.

Wu W. 2001, CCHE2D Sediment Transport Model (Version 2.1), Tech. Rep. No. NCCHE-TR-2001-3, National Center for Computational Hydroscience and Engineering, Univ. of Mississippi, Ole Miss, Oxford, Miss.

Wu W. and Vieira D. A. 2000, One-dimensional channel network model CCHE1D 2.0 Technical manual. Technical Report No. NCCHE-TR-2000-1, National Centre for Computational Hydroscience and Engineering, The University of Mississippi.

Yalin M. S. 1970, Theory of Hydraulic Models. Macmillan, London.

Yang C. T. 1973, Incipient motion and sediment transport. Journal of Hydraulic Div., Am. Soc. Civ. Eng., Vol. 99, No. 10, pp. 1679–1704.